

# Time-dependent orbital-free density functional theory for electronic stopping power: Comparison to the Mermin-Kohn-Sham theory at high temperatures

Alexander J. White,<sup>1</sup> Ondrej Certik,<sup>2</sup> Y. H. Ding,<sup>3</sup> S. X. Hu,<sup>3</sup> and Lee A. Collins<sup>1</sup>

<sup>1</sup>Theoretical Division, Los Alamos National Laboratory, Los Alamos, New Mexico 87545, USA

<sup>2</sup>Computational Computer Science Division, Los Alamos National Laboratory, Los Alamos, New Mexico 87545, USA

<sup>3</sup>Laboratory for Laser Energetics, University of Rochester, 250 E. River Road, Rochester, New York 14623, USA



(Received 5 August 2018; published 2 October 2018)

Electronic stopping power in warm dense matter can affect energy transport and heating in astrophysical processes and internal confinement fusion. For cold condensed matter systems, stopping power can be modeled from first-principles using real-time time-dependent density functional theory (DFT). However, high temperatures (10's to 100's of eV) may be computationally prohibitive for traditional Mermin-Kohn-Sham DFT. New experimental measurements in the warm dense regime motivates the development of first-principles approaches, which can reach these temperatures. We have developed a time-dependent orbital-free density functional theory, which includes a novel nonadiabatic and temperature-dependent kinetic energy density functional, for the simulation of stopping power at any temperature. The approach is nonlinear with respect to the projectile perturbation, includes all ions and electrons, and does not require *a priori* determination of screened interaction potentials. Our results compare favorably with Kohn-Sham for temperatures in the WDM regime, especially nearing 100 eV.

DOI: [10.1103/PhysRevB.98.144302](https://doi.org/10.1103/PhysRevB.98.144302)

## I. INTRODUCTION

Stopping of high-energy ions by materials is relevant to many applications, from biomedical imaging (proton computed tomography) [1], ion therapies [2,3], radiation protection, and damage [4,5]. Fusion reactions create high-energy projectiles (e.g.,  $\alpha$  particle, proton, deuterons) that deposit energy into the dense plasma as they are stopped. Accurate modeling of plasma stopping power is thus a key component for hydrodynamic modeling of internal confinement fusion (ICF) [6–11], astrophysical [12], and other fusion processes. These processes often occur inside or traverse the warm dense matter (WDM) range of densities and temperatures. In this regime, also known as the degenerate plasma, quantum mechanical processes dominate the electronic properties, while the nuclei can be treated as classical particles, and can make calculation of electronic stopping power, and other electronic response properties such as thermal and electrical conductivity a difficult task.

For slow projectile velocities ( $v_p$ ), much less than the Fermi velocity,  $v_p \ll v_F$ , Born-Oppenheimer molecular dynamics, where the electrons are in their instantaneous thermal equilibrium state, can be utilized to calculate the ionic stopping [13]. For high-velocity projectiles, with keV to MeV kinetic energy, nonadiabatic energy loss from the nuclei to the electrons dominates stopping. Analytical approaches, based on either homogeneous or local electron densities and linear response to the projectile, are often used to estimate electronic stopping power [6,14–17]. For warm dense systems these methods can be inaccurate and often require *ad hoc* cutoffs, interpolations, or additional approximate projectile-plasma pseudointeraction potential [15,16].

Recently, an increased effort to directly simulate stopping power from first principles using time-dependent density functional theory (TD-DFT), both for low-temperature materials and in warm dense matter [18–28] has arisen. In this method the electrons are treated quantum mechanically, and the ion is treated as a classical time-dependent potential. As the projectile potential may be strongly perturbative, real-time TD-DFT is typically applied, rather than linear-response TD-DFT. A mean-field approximation, i.e., Ehrenfest, is applied to calculate the force that the electrons exert on the projectile ion.

These TD-DFT approaches employ the Kohn-Sham (KS) formulation, where the exact noninteracting kinetic energy can be determined exactly by introducing auxiliary orthogonal bands or orbitals [29]. Unfortunately, for finite-temperature KS-DFT, as determined by the Mermin extension [30], the increased number of required orbitals causes the computational cost to scale cubically with respect to temperature [31,32]. Additionally, direct simulation of stopping power requires averaging over many ion configurations, and may necessitate large simulation cells. This has prevented TD-KS-DFT from being applied to higher, ICF and warm dense matter relevant, temperatures in the mega-Kelvin region.

While more approximate, the orbital-free (OF)-DFT approach has been extremely successful for calculating equilibrium properties, e.g., equation of state and nuclear transport coefficients, of warm dense matter and non-transition-metallic materials [33–47]. This approach depends only on the electron density, as opposed to auxiliary orbitals, thus avoiding the increased computational cost for high temperatures.

There has been significant effort in the development of approximate kinetic energy density functionals (KEDFs)

for OF-DFT. *Ab initio* theory, semiempirical fitting, and machine-learning routes have all been used to determine new KEDFs [38,48–52]. Most often, these KEDFs are derived from the static Lindhard response function (LRF) for a noninteracting homogenous electron gas (NI-HEG) [53,54]. Less attention has been given to the development of dynamic KEDF's specifically targeting electronic-response properties [55,56], such as stopping power.

In this paper, we develop a time-dependent orbital-free DFT approach to directly simulate stopping power at ICF relevant temperatures. We propose a new, simple, and easily computable, dynamic KEDF derived from the dynamic LRF, with an extension to finite temperatures. This dynamic KEDF is nonadiabatic, depending on the local current density. However, it does not add significant computational cost compared to the adiabatic TD-OF-DFT, and it allows significantly longer propagation time steps. Like TD-KS-DFT, the TD-OF-DFT goes beyond linear response, includes exchange correlation effects, and uses a local or semilocal density approximation as opposed to a homogenous density approximation. The TD-OF-DFT is a first-principles, all-ion, all-electron approach. We test this new approach on the simulation of stopping power in WDM by direct comparison to TD-KS-DFT and other analytical approaches.

The paper is organized as follows: we review orbital-free DFT theory for equilibrium/ground state with the static Thomas-Fermi–von-Weizsäcker KEDF, which is derived from the static LRF in Appendix A. Then the general extension of OF-DFT to TD-OF-DFT is presented, and we derive our nonadiabatic, current-dependent, KEDF from the dynamic LRF at zero temperature. This KEDF is generalized to finite temperatures by fitting to numerical calculations of the finite-temperature dynamic LRF. Finally, we apply this formalism to simulate stopping power in warm dense deuterium, which has been previously calculated using TD-KS-DFT, and compare adiabatic OF, nonadiabatic OF, and KS results to analytical results including the Brown-Preston-Singleton (BPS) [14], Li-Petrasso (LP) [6], and dielectric function (DF) [16] approach. We utilize atomic units and notations in this paper,  $e = 1$ ,  $\hbar = 1$ ,  $m_e = 1$ , and  $4\pi\epsilon_0 = 1$ .

## II. METHODOLOGY

### A. Thomas-Fermi–von-Weizsäcker kinetic energy functional

For time-independent DFT, one must minimize the total electronic free-energy functional:

$$F[\rho] = K[\rho] + \int V_{\text{ext}}(\mathbf{r})\rho(\mathbf{r})d\mathbf{r} + \frac{1}{2} \int V_H[\rho, \mathbf{r}]\rho(\mathbf{r})d\mathbf{r} + E_{XC}[\rho], \quad (1)$$

under a constant particle number constraint. This leads to a minimization of the constrained functional

$$\Omega[\rho] = F[\rho] - \mu \left( \int \rho(\mathbf{r})d\mathbf{r} - N \right). \quad (2)$$

Physically,  $\mu$  is the electronic chemical potential,  $\rho(\mathbf{r})$  is the total electron density,  $K[\rho, \mathbf{r}]$  and  $E_{XC}[\rho, \mathbf{r}]$  are the kinetic and exchange correlation energy functionals.  $V_{\text{ext}}(\mathbf{r})$  and

$V_H(\rho, \mathbf{r})$  are the external and mean-field Hartree potentials.  $F[\rho]$  is the system free energy. We utilize the Perdew and Zunger local exchange correlation functional,  $E_{XC}$  [57].

In Kohn-Sham DFT the kinetic energy is given by introducing auxiliary noninteracting orbitals,  $\rho(\mathbf{r}) = \sum_i f_i \phi_i(\mathbf{r})^* \phi_i(\mathbf{r})$  and  $K = \sum_i f_i \phi_i(\mathbf{r}) \frac{-\nabla^2}{2} \phi_i(\mathbf{r})$ . In the Mermin formulation [30],  $f$  is a Fermi-Dirac distribution function (at  $T = 0$ ,  $f_i = 2$  if  $i < \frac{N}{2}$ ). For large  $T$  or  $N$  this approach can become computationally prohibitive.

In the Thomas-Fermi–von-Weizsäcker theory, the kinetic energy density functional is given by

$$K[\rho] \approx K_{TF}[\rho] + \frac{1}{8C_{VW}} \frac{|\nabla\rho(\mathbf{r})|^2}{\rho(\mathbf{r})}. \quad (3)$$

$C_{VW}$  ranges from 1–9 depending whether the von Weizsäcker term is derived as a high wave vector asymptotic limit or a gradient correction to the Thomas-Fermi functional (low wave vector), see Appendix A [52,58]. The relationship between this orbital-free approach and the Kohn-Sham approach can be more clearly seen by expressing the density as  $\rho(\mathbf{r}) \equiv \phi(\mathbf{r})^2$ . Then Eq. (4) can be equivalently expressed as

$$K_{TFW}[\phi] = K_{TF}[\phi] + \frac{1}{C_{VW}} \phi(\mathbf{r}) \frac{-\nabla^2}{2} \phi(\mathbf{r}). \quad (4)$$

Thus the electrons are treated by a single, bosonlike, collective orbital,  $\phi$ , with  $K_{TF}[\phi]$  compensating for the free-energy increase due to the fermionic nature of electrons.

Inserting  $\phi$  into Eq. (2), we can write the minimization as an eigenvalue problem, similar to the Kohn-Sham approach:

$$\mu\phi(\mathbf{r}) = \frac{\delta F[\rho]}{\delta\rho(\mathbf{r})} \phi(\mathbf{r}), \quad (5)$$

where  $\mu$  and  $\phi$  are the lowest eigenvalue and corresponding eigenvector. The functional derivative  $\frac{\delta F[\rho]}{\delta\rho(\mathbf{r})}$  can be found self-consistently, by conjugate gradient minimization [59], or by using the imaginary time method for finding the lowest eigenvalue,

$$-\frac{\partial\phi(\mathbf{r}, \tau)}{\partial\tau} = \frac{\delta F[\rho(\tau)]}{\delta\rho(\mathbf{r})} \phi(\mathbf{r}, \tau), \quad \tau \rightarrow -i\infty, \quad \phi(\mathbf{r})^2 = N. \quad (6)$$

### B. Time-dependent orbital-free: Thomas-Fermi–von-Weizsäcker

The calculation of dynamic electron response properties requires a time-dependent electronic structure approach. Extension of the OF method to time-dependent densities requires calculation of the current density or electron velocity field. This can be accomplished by introducing a complex collective orbital, the Madelung wave function [60], which is defined by the time-dependent density and longitudinal current, as required by the Runge-Gross Theorem [61],

$$\begin{aligned} \phi(\mathbf{r}, t) &\equiv e^{iS(\mathbf{r}, t)} \sqrt{\rho(\mathbf{r}, t)} \\ i\dot{\phi}(\mathbf{r}, t) &= [-\nabla^2/2 + \hat{V}(\mathbf{r}, t)]\phi(\mathbf{r}, t), \\ \hat{V}(\mathbf{r}) &= \frac{\delta K_{TF}[\rho]}{\delta\rho(\mathbf{r}, t)} + V_H(\mathbf{r}, t) + V_{\text{ext}}(\mathbf{r}, t) + \frac{\delta E_{XC}[\rho]}{\delta\rho(\mathbf{r}, t)}, \\ \mathbf{J}(\mathbf{r}, t) &= \rho(\mathbf{r}, t)\nabla S(\mathbf{r}, t). \end{aligned} \quad (7)$$

This time-dependent Schrödinger-like form is utilized for computational convenience. Here,  $\mathbf{J}(\mathbf{r}, t)$  is the electronic current density and  $\nabla S(\mathbf{r}, t)$  is the electronic velocity field. A hydrodynamic form with two real valued equations of motion for  $\rho$  and  $\mathbf{J}$  would be equivalent [60,62]. The Laplacian term in Eq. (7) accounts for both the static von-Weizsäcker KED potential and the high-frequency limit dynamic KED response, shown below [63]. More specifically it leads to the quantum Bohmian pressure, the continuity equation, and the bulk hydrodynamic response to a potential or pressure, for the electron liquid [63–69]. We refer to the solution of Eq. (7) as the Thomas-Fermi–von-Weizsäcker (TFW), or adiabatic, version of TD-OF-DFT.

A split-operator Fourier transform approach is utilized to propagate Eq. (7) for the periodic systems presented in this paper. Classical equations of motion are used to propagate the projectile ion, with a mean-field force (Ehrenfest dynamics) based on the instantaneous average electron density,  $\rho(\mathbf{r}, t)$ , detailed in Sec. II E.

In Appendix A, we review how the TFW functionals can be derived from the static LRF for the NI-HEG. In the next section we derive an additional dynamic kinetic energy density potential (KEDP) by following a similar procedure for the dynamic LRF.

### C. Dynamic kinetic energy functional from Lindhard response

For finding a dynamic KEDP, we follow the same strategy as outlined in Appendix A. That is, we seek a functional derivative, which would closely approximate the dynamic LRF,  $\chi_L$ , i.e.,

$$\frac{\delta E_{\text{kin}}[\rho]}{\delta \rho(\mathbf{r}, t)} = - \int d\mathbf{r}' \int dt' \chi_L^{-1}(\mathbf{r}, \mathbf{r}', t, t') \delta \rho(\mathbf{r}', t'). \quad (8)$$

However, implementing a nonlocal functional, in space and time, would add considerable expense when compared to the TFW formulation [55]. We seek a local current-density KEDF, thus we further approximate that the electron density does not change rapidly with time or space, so the  $\chi_L$  is the response of a NI locally HEG and

$$\begin{aligned} \chi_L(\mathbf{r}, \mathbf{r}', t, t') &\approx \chi_L(\mathbf{r}, |\mathbf{r} - \mathbf{r}'|, t, t - t') \\ &\equiv \mathcal{F}^{-1}[\tilde{\chi}_L(\mathbf{r}, q, t, \omega)], \end{aligned} \quad (9)$$

where the time and space dependence of the response function comes from the Fermi wave vector/momentum ( $k_F$ ) density dependence:

$$k_F \rightarrow K_F(\mathbf{r}, t) = [3\pi^2 \rho(\mathbf{r}, t)]^{1/3}, \quad (10)$$

and  $\mathcal{F}$  is the Fourier transform in space and time. The reciprocal space variables and functions are defined by:  $i\omega \tilde{F}(\omega) = \mathcal{F}_{\omega, t}[\frac{d}{dt} F(t)]$  and  $i q \tilde{F}(q) = \mathcal{F}_{q, r}[\frac{d}{dr} F(r)]$ , for any real space and time dependent function,  $F$ , and reciprocal function,  $\tilde{F}$ .

Since we are assuming a slowly varying density, we will expand the density in time,  $t'$  around  $t$ , and only keep the first order,

$$\begin{aligned} \delta \rho(\mathbf{r}', t') &\approx \delta \rho(\mathbf{r}', t) + \frac{\partial \rho(\mathbf{r}', t)}{\partial t} (t - t') \\ \frac{\partial \rho(\mathbf{r}', t)}{\partial t} &= -\nabla \cdot \mathbf{J}(\mathbf{r}', t). \end{aligned} \quad (11)$$

Then the right-hand side of Eq. (8) becomes

$$\begin{aligned} & - \int d\mathbf{r}' \delta \rho(\mathbf{r}', t) \int d(t - t') \chi_L^{-1}(\mathbf{r}, \mathbf{r} - \mathbf{r}', t, t - t') \\ &= -\mathcal{F}_{q, r}^{-1}[\tilde{\chi}_L^{-1}(\mathbf{r}, \mathbf{r}, \mathbf{q}, \omega = 0) \delta \rho(\mathbf{q}, t)]. \end{aligned} \quad (12)$$

This, fully local temporal, approximation to the density leads to the static/adiabatic TFW functionals.

The second term in Eq. (11), which leads to our current-dependent KEDF, can be represented in reciprocal space by

$$\begin{aligned} & - \int d\mathbf{r}' \frac{\partial \rho(\mathbf{r}', t)}{\partial t} \int d(t - t') (t - t') \chi_L^{-1}(\mathbf{r}, \mathbf{r} - \mathbf{r}', t, t - t') \\ &= - \int d\mathbf{r}' \left[ \frac{-i \partial \chi_L^{-1}(\mathbf{r}, \mathbf{r} - \mathbf{r}', t, \omega)}{\partial \omega} \right]_{\omega \rightarrow 0} \nabla \cdot \mathbf{J}(\mathbf{r}', t). \\ &= -\mathcal{F}_{q, r}^{-1} \left[ \frac{-i \partial \tilde{\chi}_L^{-1}(\mathbf{r}, \mathbf{q}, t, \omega)}{\partial \omega} \Big|_{\omega \rightarrow 0} i \mathbf{q} \cdot \tilde{\mathbf{J}}(\mathbf{q}, t) \right]. \end{aligned} \quad (13)$$

We can take limits in  $\omega$  and  $q$  of the Fourier transformed,  $\tilde{\chi}_L(q, \omega)$ ,

$$\begin{aligned} -i \frac{\partial \tilde{\chi}_L^{-1}(q, \omega)}{\partial \omega} \Big|_{\substack{\omega \rightarrow 0 \\ q \rightarrow 0}} &\approx -\frac{\pi^2}{k_F} \left[ \frac{\pi}{2k_F q} + \dots \right] \\ -i \frac{\partial \tilde{\chi}_L^{-1}(q, \omega)}{\partial \omega} \Big|_{\substack{\omega \rightarrow 0 \\ q \rightarrow \infty}} &= 0. \end{aligned} \quad (14)$$

Replacing  $k_F$ , with  $K_F(\mathbf{r}, t)$  and keeping only the lowest order in  $q$ , leads to our local current-dependent (CD) kinetic energy density potential (KEDP, functional derivative of KEDF),

$$V_{\text{CD}}(\mathbf{r}, t) = \frac{\pi^3}{2K_F^2(\mathbf{r}, t)} \mathcal{F}_{q, r}^{-1}[i \mathbf{q} \cdot \tilde{\mathbf{J}}(\mathbf{q}, t)/|q|](\mathbf{r}). \quad (15)$$

In the high-frequency limit,

$$\tilde{\chi}_L^{-1}(q, \omega \rightarrow \infty) = \frac{3\pi^2 \omega^2}{k_F^3 q^2} = \frac{\omega^2}{\rho q^2}, \quad (16)$$

which is the result of the bulk hydrodynamic response of the current to a potential or vector potential:

$$\begin{aligned} \delta \tilde{\mathbf{J}}(\mathbf{r}, t) &= -\rho(\mathbf{r}, t) \nabla \delta V(\mathbf{r}, t), \\ \delta \mathbf{J}(\mathbf{r}, t) &= -\rho(\mathbf{r}, t) \delta \mathbf{A}(\mathbf{r}, t), \end{aligned} \quad (17)$$

and is satisfied by the Laplacian operator in Eq. (7) [63]. We refer to the solution to Eq. (7) with the addition of the CD KEDP in Eq. (15) to  $\hat{V}(\mathbf{r}, t)$  as the current-dependent (CD), or nonadiabatic, version of TD-OF-DFT.

We consider two approximate inverse response function for the NI-HEG:

$$\tilde{\chi}_{TFW}^{-1}(q, \omega) = -\frac{\pi^2}{k_F} \left[ 1 + \frac{3q^2}{4k_F^2} - \frac{3\omega^2}{k_F^2 q^2} \right] \quad (18)$$

$$\tilde{\chi}_{\text{CD}}^{-1}(q, \omega) = \tilde{\chi}_{TFW}^{-1}(q, \omega) + i \frac{\pi^3 \omega}{2k_F^2 q}. \quad (19)$$

Propagation of a linearly perturbed NI-HEG by Eq. (7) will result in the response  $\tilde{\chi}_{TFW}(q, \omega)$ . Addition of the dynamic KEDP will result in the response  $\tilde{\chi}_{\text{CD}}(q, \omega)$ . Comparison of  $\tilde{\chi}_{\text{CD}}(q, \omega)$  and  $\tilde{\chi}_{TFW}(q, \omega)$  to the exact LRF,  $\tilde{\chi}_L(q, \omega)$

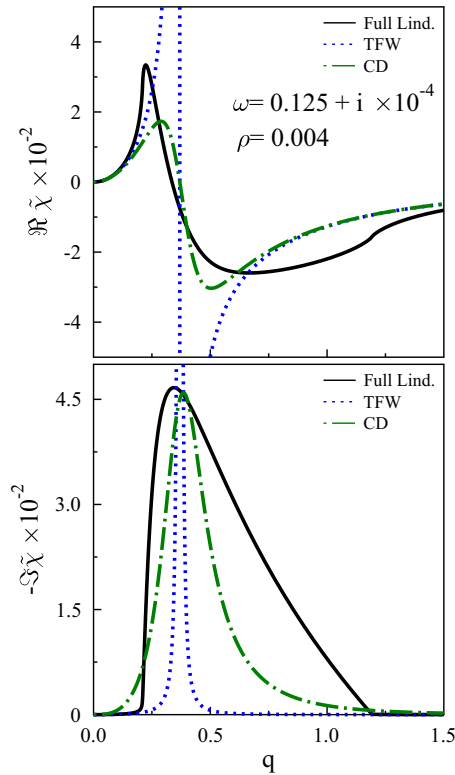


FIG. 1. Dynamic density-density response functions for homogeneous electron gas as a function of wave vector. The electron density,  $\rho = 0.004$  gives a Fermi-wave vector,  $k_F = 0.491$ . The frequency is  $\omega = 0.125 + i \times 0.0001 \sim k_F^2/2 + i\delta$ , Lindhard response function (black solid), Thomas-Fermi-von-Weizsäcker response (blue dotted), the current-dependent response (green dash-dot).

at finite  $\omega$  are shown in Fig. 1. Both response functions have a resonance/singularity at  $\frac{\omega}{k_F} = \pm \frac{q}{k_F} \sqrt{\frac{1}{3} + \left(\frac{q}{2k_F}\right)^2}$ , but the  $\tilde{\chi}_{CD}(q, \omega)$  resonance is broadened by the imaginary term in Eq. (19). The real-time effect of the CD KEDP,  $V_{CD}$ , is then to dampen density oscillations, i.e., longitudinal  $\mathbf{J}(\mathbf{r}, t)$ . This dampening is caused by the decay of the bulk hydrodynamic motion into electron-hole excitations/individual electron motions. In the TD-KS-DFT approach, these single-particle excitations/motions are resolved by the introduction of the auxiliary orbitals. The role of the CD KEDP is to effect these individual motions/excitations. Differences between  $\tilde{\chi}_{CD}$  and  $\tilde{\chi}_L$  are due to the semilocal approximations in  $\tilde{\chi}_{CD}^{-1}$ .

In previous work [55], Neuhauser *et al.* determined a KEDP with a comparable approximate response function, i.e., Fig. 1 can be compared to Figs. 1 and 2 of Ref. [55]. In Ref. [55], 14–28 fits of the LRF are utilized, each with eight parameters. For each fit a corresponding field requires propagation in time, using Fourier transforms. This adds considerable cost and complication compared to  $V_{CD}$ , determined only by the low and high limits of  $\omega$  and  $q$ , which requires one Fourier transform of the current, and one inverse Fourier transform to generate the real-space potential. The simple form of  $V_{CD}$  also allows for a straightforward extension to finite temperatures, critical to simulations in warm dense matter.

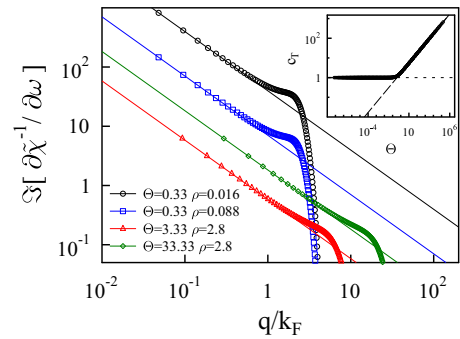


FIG. 2.  $\Im[\frac{\partial \tilde{\chi}_L^{-1}(q, \omega, T)}{\partial \omega}]_{\omega \rightarrow 0}$  as a function of the scaled wave vector  $q/k_F$ . Four density-temperature examples are shown. Markers are numerical calculations of Eq. (20) and its derivative, lines are calculated by Eqs. (21) and (24). The inset shows the best fits of the scaling factor  $c_T$  to the  $\Im[\frac{\partial \tilde{\chi}_L^{-1}(q, \omega, T)}{\partial \omega}]_{\omega \rightarrow 0}$  v.s.  $q$  lines compared to the asymptotic limit fits, Eqs. (22) and (23), as well as the final  $c_T$ , Eq. (24).

Similar approaches have been followed looking to determine the nonadiabatic friction due to exchange and correlation, which is neglected here. Nazarov *et al.* have demonstrated the importance of nonadiabatic exchange correlation on stopping of slow ions by electron liquids/gas [70,71]. Here, we focus only on the friction due to the noninteracting electrons, which is described exactly by adiabatic Kohn-Sham and approximately by our orbital-free approach.

#### D. Temperature-dependent dynamic kinetic energy functional

For either OF or KS-DFT simulations, the temperature dependence of the KEDF must be accounted for when  $k_B T$  is on the electronic energy scales (typically eV or greater). For KS-DFT, the Mermin approach is a straightforward, but often computationally prohibitive, extension of the time-dependent or independent case to any temperature. For time-independent OF-DFT, Perrot determined analytic functional forms for the temperature dependence of the free energy of the NI locally HEG, as well as the corresponding gradient expansion [51].

For time-dependent OF-DFT, we must generalize the dynamic kinetic energy potential to finite temperatures. We assume a parametric dependence on temperature, consistent with an isothermal ensemble. Unfortunately the finite-temperature Lindhard function is not generally analytically solvable. However, it can be calculated numerically using [64]

$$\tilde{\chi}_L(q, \omega, T) = \int_0^\infty dE \frac{\tilde{\chi}_L(q, \omega, T=0, k_F = \sqrt{2E})}{4k_B T \cosh^2\left(\frac{E - \mu(T)}{2k_B T}\right)}, \quad (20)$$

where  $\mu(T)$  is the NI-HEG chemical potential [51]. At high temperatures,  $k_B T \gg \frac{k_F^2}{2}$ , we find as  $q \rightarrow 0$ ,

$$-i \frac{\partial \tilde{\chi}_L^{-1}(q, \omega = 0, T)}{\partial \omega} \approx -\frac{\pi^2}{k_F} \left[ \frac{\pi}{2k_F q} \right] \times c_T, \quad (21)$$

where

$$c_T = \Theta^{1/2} \times 1.69271 \left( \Theta = \frac{2k_B T}{k_F^2} \rightarrow \infty \right). \quad (22)$$

For low temperatures

$$c_T = 1 \quad (\Theta \rightarrow 0). \quad (23)$$

For arbitrary  $k_B T$  we take

$$c_T = ([\Theta^{1/2} \times 1.69271]^{3.6} + 1)^{\frac{1}{3.6}}. \quad (24)$$

The two numerical constants in  $c_T$  are determined by fitting calculations of  $\Im[\frac{\partial \tilde{\chi}_E^{-1}(q, w, T)}{\partial w}]_{\omega \rightarrow 0}$  as a function of  $q$  for 441 temperature and electronic density points spanning the warm dense matter regime,  $0.27 \text{ meV} < k_B T < 86.2 \text{ keV}$  and  $0.1 \text{ g/cc} < \rho \times \frac{m_p}{m_e} < 10000 \text{ g/cc}$ . Four of these fits are shown in Fig. 2. Best fits of  $c_T$  for individual  $\rho - k_B T$  points are shown in the inset of Fig. 2, along with the limits [Eqs. (22) and (23)] and the final form [Eq. (24)]. We then assume a local density approximation for  $c_T \rightarrow C_T(\mathbf{r}, t)$  as well by using the local  $K_F(\mathbf{r}, t)$  in place of the average  $k_F$ . The temperature-dependent CD potential is then given by

$$V_{\text{CD}}(\mathbf{r}, t, T) = C_T(\mathbf{r}, t) \times V_{\text{CD}}(\mathbf{r}, t, T = 0). \quad (25)$$

### E. Simulation of electronic stopping power

We perform direct simulation of the electronic stopping power following Ref. [21]. First, a time-independent OF molecular dynamics simulation is run to determine snapshots of the ionic configurations, and the corresponding equilibrium electronic density. To initialize the stopping power simulation we insert an extra ion (the projectile) on one side of the periodic box with a constant velocity,  $v_p$ . All other ions (the bulk) have a fixed position. Fixing the positions of the bulk nuclei and the velocity of the projectile separates the electronic contribution to the stopping power from the nuclear contribution [21]. Then the electronic density and current are propagated according to Eq. (7) with (CD) or without (TFW)  $V_{\text{CD}}(\mathbf{r}, t)$  added to  $\hat{V}(\mathbf{r}, t)$ . The projectile is propagated by Newton's equations using a mean-field force of the electrons.

For simulations with a local electron-ion potential or pseudopotential, in either the KS or OF approach, the total mean-field force on the projectile is simple to calculate, due to the Hellmann-Feynman theorem,

$$F_p[\rho, \mathbf{R}] = \frac{\partial V_{ii}(\mathbf{R})}{\partial R_p} + \int d\mathbf{r} \rho(\mathbf{r}) \frac{\partial V_{ie}(\mathbf{R})}{\partial R_p}. \quad (26)$$

$\mathbf{R}$  are the nuclear coordinates, and  $p$  indexes the projectile nuclei. For periodic simulations with fixed bulk nuclei and a fixed projectile velocity, the contribution from  $\frac{\partial V_{ii}(\mathbf{R})}{\partial R_p}$  to the time average of  $F_p$  will net to zero. Thus we simulate only electronic stopping power. Note that ionic stopping power can be simulated from Born-Oppenheimer dynamics, while full ionic-electronic stopping power can be simulated by allowing the bulk nuclei to move. However, at these projectile velocities, electronic stopping power is the dominant contribution and our targeted quantity. The recent review by Correa contains a detailed description of ionic and electronic contributions to stopping power [72]. The work,  $W_p$ , done on

the projectile, and the electronic stopping power (ESP) can be calculated as:

$$W_p = - \int dt F_p[\rho, \mathbf{R}, t] \cdot \mathbf{v}_p \quad (27)$$

$$= - \int F_p[\rho, \mathbf{R}, t] \cdot dR_p, \text{ and} \quad (28)$$

$$\text{ESP} = \left\langle \frac{dW_p}{dR_p} \right\rangle = - \langle F_p[\rho, \mathbf{R}, t] \rangle. \quad (29)$$

An example of the work calculated for during a trajectory is shown and discussed in Appendix B.

### III. APPLICATION TO DEUTERIUM: LOW TEMPERATURES

We compare the real time OF and KS stopping power simulations for a deuteron stopped by bulk deuterium. This system has been previously investigated using real-time TD-KS-DFT by Magyar *et al.* [21] Following Ref. [21] we utilize a cubic simulation cell with 128 bulk ions. Unlike Ref. [21] we do not eliminate trajectories that have close passes between the projectile and bulk ions. We have recalculated the Kohn-Sham results so that we can compare to the orbital-free simulations without any additional sensitivities to the pseudopotential and real-time propagation method, for example. Initial equilibrium Mermin-Kohn-Sham calculations are performed using the AB-INIT software package [73]. Real-time propagation of the resulting orbitals is performed separately.

For each ESP calculation, three OFMD snapshots are taken. For each snapshot, multiple initial positions of the projectile are sampled, ten for current-dependent orbital-free, five for TFW, and four for Kohn-Sham. Each of these trajectories is composed of at least three passes through the unit cell with the first pass discarded from the average in Eq. (29) [21]. Note that these simulations, while resolved with respect to sampling of initial conditions, are not necessarily resolved with respect to simulation box size for high velocities ( $v_p \gg v_F = [3\pi\bar{\rho}]^{1/3}$ ). This is discussed in detail in Appendix C. While TD-OF-DFT can be used with simulation box sizes required to converge the high-velocity stopping power, as has been shown in our previous work [74], it is not currently feasible for TD-KS-DFT. This is due to scaling of the computational cost with respect to the required number of orbitals. The TD-OF scales with the volume/grid, but the TD-KS scales with the volume/grid and the number of orbitals.

Stopping power at temperatures of 10 and 100 kK and a density of 0.7 g/cc deuterium are shown in Fig. 3. Compared to KS, the OF approaches overestimates the stopping power at the Bragg peak. However, they quickly converge to agreement at higher velocities. The CD potential significantly improves the low-velocity stopping power, compared to TFW, which shows a sharp drop in stopping power at low velocities. Since dissipation of the net electronic current due to electron-hole excitations (imaginary part of the LRF) is effected by the CD potential, we conclude that electron-hole excitations are the dominant mechanism for electronic stopping in low-velocity projectiles. The 10 and 100 kK simulations are low-temperature simulations compared to typically accepted limits for accurate ground-state orbital-free DFT with TFW

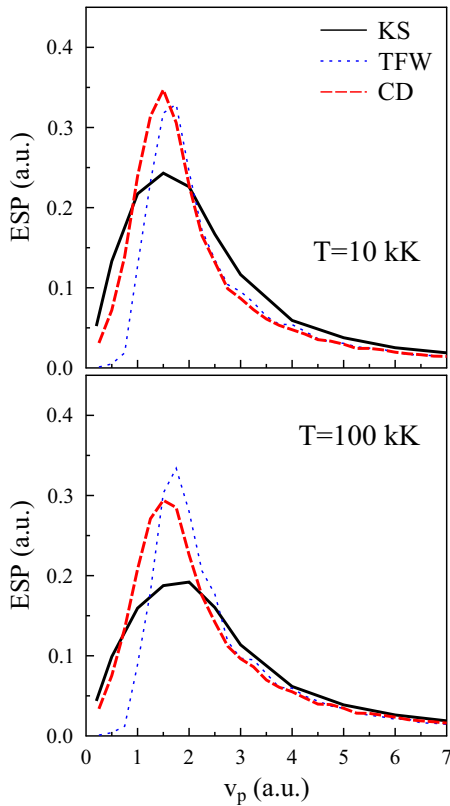


FIG. 3. 0.7 g/cc deuterium stopping power (ESP) for deuteron. Top:  $10^4$  Kelvin; bottom:  $10^5$  Kelvin. Time-dependent (TD) Kohn-Sham (black solid); current-dependent TD orbital-free (CD) (red fashed); TFW TD orbital-free (blue dotted).

functionals. Thus the qualitative agreement at low projectile velocities, and quantitative at high velocities, is highly encouraging.

#### IV. APPLICATION TO DEUTERIUM: HIGH TEMPERATURES

To determine the effect of increasing temperature on DFT stopping power, we perform a series of simulations ranging from 10–100 kilo-Kelvin (8.6–86 eV). Due to the high cost of Mermin-Kohn-Sham equilibrium and real-time time-dependent DFT calculations at high temperatures, we must reduce the size of our simulations to a rectangular cell of 32 atoms, with twice the box length parallel to the projectile velocity compared to perpendicular directions. A single trajectory through the middle of this box is used to calculate the stopping power. While these simulations are not expected to be converged in size, or sampling of ion configurations, we again expect that the direct comparison of the KS and OF methods on the exact same trajectory to be informative. Note that some oscillations appear in the Kohn-Sham result due to the small box size. Low velocities, near or lower than the Bragg peak, are converged but high velocities are suppressed compared to converged results. In Appendix C we show dependence, up to convergence, of the TD-OF-DFT stopping power, which is currently prohibitive for the TD-KS-DFT approach at high temperatures.

#### A. LP, BPS, and DF methods

In addition to the density functional theory methods we compare to three analytical models. The Li-Petrasso (LP) model is based on the Fokker-Planck equation and includes plasma-ion stopping, collective plasma oscillation, and quantum corrections. The Brown-Preston-Singleton (BPS) method assumes a weak plasma coupling, but accounts for quantum effects and Fermi-Dirac statistics. The dielectric function (DF) approach is based on the RPA density linear response/energy loss function, but is second order in the coupling between projectile ion and the electron gas. All three assume stopping by a uniform electron density. In the LP and BPS models the projectile is assumed to be a bare ion, with no screening from bound electrons. We have performed two instances of the DF method, following Ref. [16] one with the bare ion, and another with screening from bound electrons,  $\tilde{\rho}_p(q)$ .  $\tilde{\rho}_p(q)$  is calculated from an average-atom Thomas-Fermi-Dirac model [75]. The BPS and LP methods are most appropriate for nearly ideal plasmas, low density and/or high temperature, while the DF is most appropriate for high but nearly uniform electron densities.

The relationship between the DFT methods and the DF approach warrants further discussion. The real-time TD-KS-DFT method takes into account the electron response to the projectile at the RPA plus approximate exchange correlation level. The DF approach is based on the RPA description of the electronic response. The TD-OF-DFT approximates the noninteracting KEDF, neglecting the fully nonlocal terms, but includes the approximate exchange correlation. However, both the TD-OF and TD-KS DFTs go beyond linear response and make approximations based on the local density, whereas the DF method assumes linear response of a homogeneous electron density. Finally, the TD-OF and TD-KS DFTs do not discriminate between the projectile and the bulk ions, in terms of the location or type of the electrons. Thus they do not require a further approximation to the bound vs free electrons of the projectile or bulk. As we see from the bare and screened DF results, projectile screening has a large effect on stopping. However, it is not easy to know the appropriate amount of screening for such a nonequilibrium process. Note, the KS simulations can, and often do, utilize pseudopotentials to account for some bound electrons, with strong implications for stopping power [23,76,77], but all KS simulations in this paper are all-electron.

#### B. Simulation and model results

In Figs. 4 and 5 we compare the simulated deuterium stopping power from TD-KS and CD TD-OF to the commonly used, analytical, LP, BPS, and DF models, for 0.7 g/cc and 3.5 g/cc deuterium, respectively. We also calculate the CD stopping power with the temperature- and density-dependent coefficient  $C_T$  [Eq. (24)] set to one, and the DF stopping power with no screening from bound electrons [ $\rho_p(q) = 0$ ]. The high-temperature Kohn-Sham calculations become more computationally affordable for higher densities. Thus we reach 1 mega-Kelvin temperatures for the 3.5 g/cc simulation, but only 600 kilo-Kelvin for the 0.7 g/cc. The temperature-dependent CD stopping power shows improved agreement with the Kohn-Sham compared to the CD without the tem-

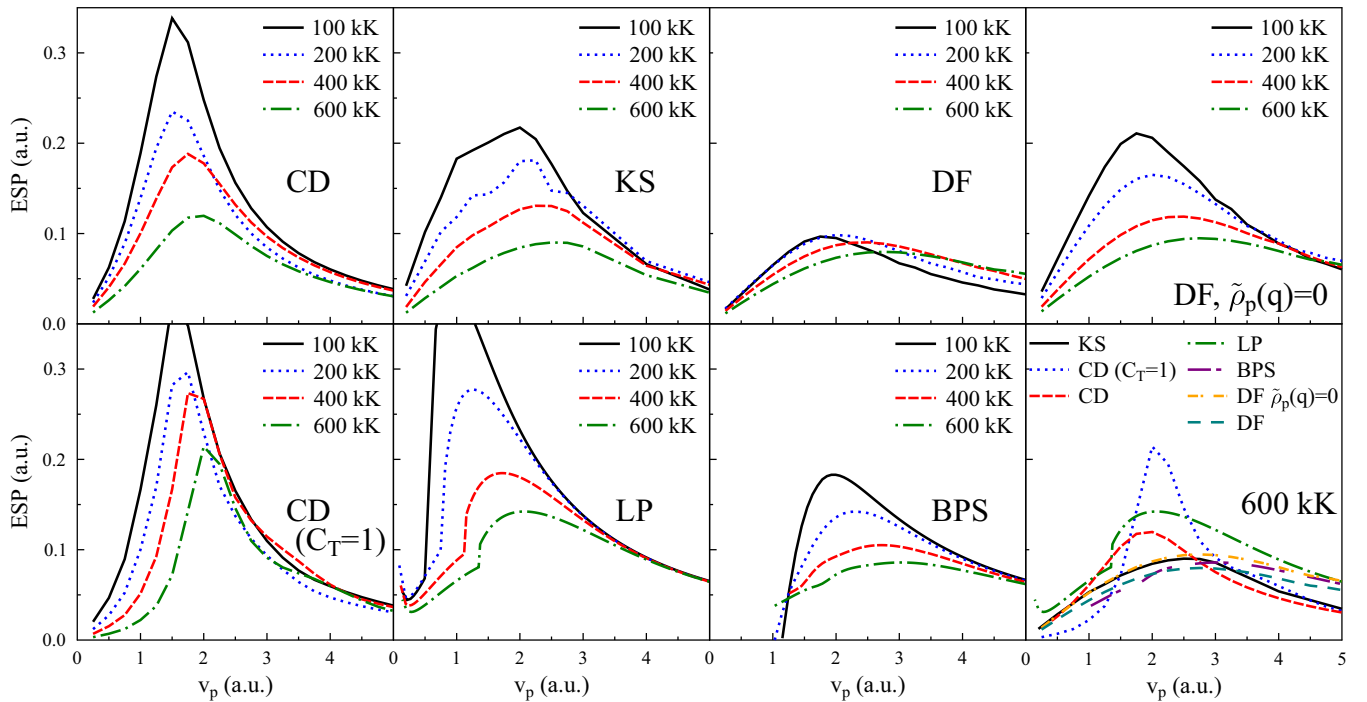


FIG. 4. 0.7 g/cc deuterium stopping power (ESP) for deuteron. Top, left: Current-dependent TD orbital-free; top, middle, left: TD Kohn-Sham; top, middle, right: dielectric function (DF) method with projectile screening; top, right: DF method with bare projectile,  $\tilde{\rho}_p(q) = 0$ . Bottom, left: Current-dependent TD orbital-free, with  $C_T = 1$ ; bottom, middle, left: Li Petrasso model; bottom, middle, right: Brown-Preston-Singleton model; bottom, right: comparison of all methods at 600000 Kelvin.

perature dependence, especially at higher temperatures, and for both densities. This provides confidence in the simple temperature dependence of the CD potential, Eq. (25). The CD result agrees with KS at high and low velocities, but overestimates at the Bragg peak. However, the agreement improves with increased temperature.

LP predicts a larger peak than the Kohn-Sham result and a discontinuous change at low velocity. The BPS peak agrees well with the KS result for near-peak velocities, but the stopping power drops significantly at low velocities, similar to what is seen in the TFW TD-OF-DFT (Fig. 3). These disagreements are not surprising given the high coupling in this system. The DF approach agrees very well with the Kohn-Sham, but only when the bound projectile electrons are not included in the calculation. The sensitivity to the DF model to the *ad hoc* treatment of the projectile electrons provides further motivation for development of the all-electron, all-ion approach of the TD-DFT methods.

The TD-DFT approaches also predict significantly lower stopping at the high-velocity tails. However, this is partially due to the small simulation box sizes, required to push the KS simulations up to such high temperatures and repeated for the OF. For high velocities, the projectile may begin to interact with its own wake in a periodic system, which results in a suppression of the stopping power. In our recent work, we found that very large boxes are required to achieve convergence for projectiles with velocities much larger than the Bragg peak [74]. However, converged results still showed  $\sim 10$ – $20$  % differences compared to the LP, BPS, DF methods, even in the 10's of MeV projectile energy regime. While the

TD-KS approach cannot simultaneously reach these box sizes and temperatures, it is based on an exact treatment of the noninteracting KEDF. Thus agreement between the TD-OF and TD-KS at these high velocities, though unconverged, still supports the verification of our previous used, and converged, TD-OF calculations [74]. We demonstrate convergence with box size for the TD-OF-DFT in Appendix C.

In Fig. 5, we show stopping power for 3.5 g/cc deuterium at 10 kK. Agreement between KS and CD is similar to the lower density case for low and high velocities, but significantly improved near the Bragg peak. This could be due to an improved orbital-free representation of the equilibrium density, due to increased ionization at higher pressure. Agreement with and between LP, BPS, and DF results is not significantly changed.

## V. CONCLUSION

We have presented a real-time time-dependent orbital-free density functional approach for calculation of electronic stopping power at high temperature. To improve numerical propagation stability as well as low projectile velocity results and temperature dependence, a dynamic, current-dependent, KEDP is required. The dynamic KEDP derived here provides the correct density-density response for a NI-HEG in the low-frequency, low wave vector limit. When this CD potential, along with the local Thomas-Fermi–von-Weizsäcker KEDP, is added to a time-dependent Schrödinger-like equation for the Madelung wave function, all high- and low-frequency and wave vector limits of the noninteracting gas response are

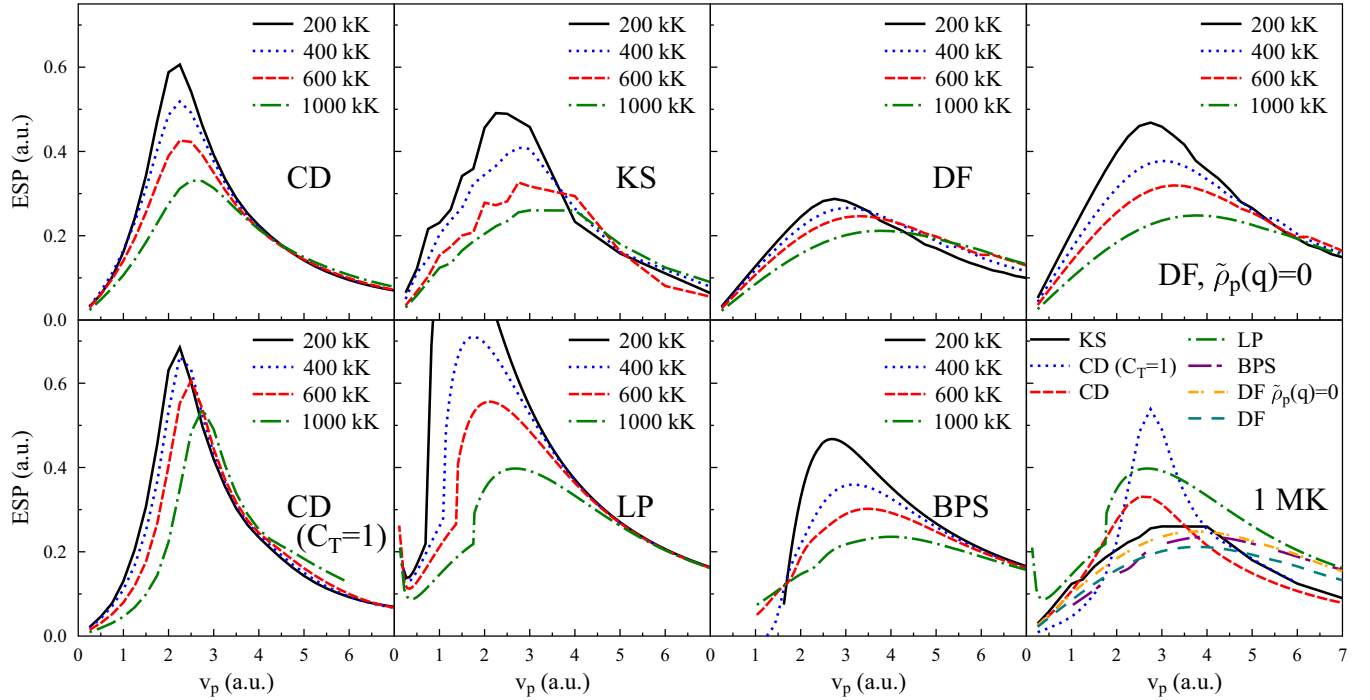


FIG. 5. 3.5 g/cc deuterium stopping power (ESP) for deuteron. Top, left: Current-dependent TD orbital-free; top, middle, left: TD Kohn-Sham; top, middle, right: dielectric function (DF) method with projectile screening; Top, right: DF method with bare projectile,  $\tilde{\rho}_p(q) = 0$ ; bottom, left: current-dependent TD orbital-free, with  $C_T = 1$ ; bottom, middle, left: Li Petrasso (LP) model; bottom, middle, right: Brown-Preston-Singleton (BPS) model; bottom, right: comparison of all methods at 1 mega-Kelvin.

reproduced. The CD orbital-free dynamics compares favorably with the real-time time-dependent Mermin-Kohn-Sham simulation of deuterium stopping power. However, it has no practical limitation on the computationally accessible temperature, and significantly reduced computational cost even for  $T = 0$ . While the TD-OF KEDF is approximate, the TD-OF-DFT approach still goes beyond linear response, accounts for the local electron density, and is an all-electron all-ion simulation. Improvement of the CD TD-OF-DFT approach may be achieved by including, already developed, nonlocal static KEDFs [54], or through future developments of dynamic KEDFs. Agreement between the bare ion DF model and the Kohn-Sham supports this claim. Future work will also include development and application of this time-dependent OF methodology to additional electronic response, e.g., conductivity, opacity, nonlinear absorption.

#### ACKNOWLEDGMENTS

The authors gratefully acknowledge support from Advanced Simulation and Computing, Science Campaign 4, computing resource from ASC, and LANL, which is operated by LANS, LLC for the NNSA of the U.S. DOE under Contract No. DE-AC52-06NA25396. This material is based upon work supported by the Department of Energy National Nuclear Security Administration under Award No. DE-NA0001944, the University of Rochester, and the New York State Energy Research and Development Authority. The support of DOE does not constitute an endorsement by DOE of the views expressed in this paper.

#### APPENDIX A: STATIC KINETIC ENERGY FUNCTIONAL FROM LINDHARD RESPONSE

Within the linear-response limit, the electronic energy functional can be derived from the density response function:

$$\partial\rho(\mathbf{r}, t) = \int d\mathbf{r}' \int dt' \chi(\mathbf{r}, \mathbf{r}', t, t') \partial V(\mathbf{r}', t), \quad (\text{A1})$$

$$\frac{\delta E[\rho]}{\delta\rho(\mathbf{r}, t)\delta\rho(\mathbf{r}', t')} = -\chi^{-1}(\mathbf{r}, \mathbf{r}', t, t'). \quad (\text{A2})$$

The KEDF, Eq. (4), can be derived from the LRF,  $\chi_L$ , of a isotropic NI-HEG. The real and imaginary parts of the Fourier transform of the Lindhard function,  $\tilde{\chi}_L$ , are given, at zero temperature, by

$$\Re[\tilde{\chi}_L](q, \omega) = -\frac{k_F}{\pi^2} \left\{ \frac{1}{2} - \frac{1-v_-^2}{4\bar{q}} \ln \left| \frac{v_-+1}{v_- - 1} \right| + \frac{1-v_+^2}{4\bar{q}} \ln \left| \frac{v_++1}{v_+ - 1} \right| \right\} \text{ and} \quad (\text{A3})$$

$$\Im[\tilde{\chi}_L](q, \omega) = -\frac{k_F}{\pi^2} \frac{\pi}{4\bar{q}} \{ (1-v_-^2)\Theta[1-v_-^2] - (1-v_+^2)\Theta[1-v_+^2] \}, \quad (\text{A4})$$

where

$$v_{\pm} = \frac{\omega}{qv_f} \pm \frac{q}{2k_F}, \quad \bar{q} = \frac{q}{k_F} \quad \text{and} \quad v_f = \frac{k_F}{m_e}. \quad (\text{A5})$$

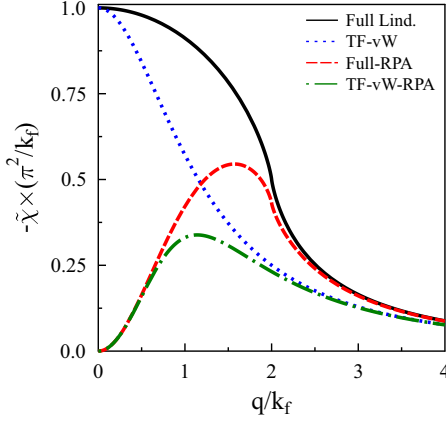


FIG. 6. Static density-density response functions for homogeneous electron gas as a function of normalized wave vector. Lindhard function (black solid), Thomas-Fermi-von-Weizsäcker (TFW) (blue dotted), random phase approximation (RPA) (red dashed), and the approximate RPA with TFW for the noninteracting response.

In the static limit,  $\omega = 0$ , relevant to the time-independent energy,

$$\Re[\tilde{\chi}_L](q, 0) = -\frac{k_F}{\pi^2} \left\{ \frac{1}{2} + \frac{\bar{q}^2 - 4}{8\bar{q}} \ln \left| \frac{\bar{q} - 2}{\bar{q} + 2} \right| \right\} \text{ and} \\ \Im[\tilde{\chi}_L](q, 0) = 0. \quad (\text{A6})$$

For nearly uniform perturbation,  $q \rightarrow 0$ , up to second order,

$$-\tilde{\chi}_L^{-1}(q, 0) = \frac{\pi^2}{k_F} \left\{ 1 + \frac{q^2}{12} \right\}. \quad (\text{A7})$$

The first term gives the Thomas-Fermi response, the second term the von-Weizsäcker response with  $C_{VW} = 9$ . In the limit of rapid oscillations in the perturbation,  $\frac{1}{q} \rightarrow 0$ ,

$$-\tilde{\chi}_L^{-1}(q, 0) = \frac{\pi^2}{k_F} \left\{ \frac{3}{5} + \frac{3q^2}{4} \right\}. \quad (\text{A8})$$

The first term is 3/5ths of the Thomas-Fermi response, the second is the full von Weizsäcker response,  $C_{VW} = 1$ . The response function, which leads to our TFW functional,

$$-\tilde{\chi}_{TF,vW}^{-1}(q, 0) = \frac{\pi^2}{k_F} \left\{ 1 + \frac{3q^2}{4} \right\}, \quad (\text{A9})$$

which best reproduces both asymptotic limits of full static Lindhard function, without requiring more computationally expensive nonlocal functionals, see Fig. 6.

## APPENDIX B: STABILITY OF TFW COMPARED TO CURRENT-DEPENDENT

Figure 7 shows a comparison of the work done on the projectile as a function of distance calculated using TD-KS and CD TD-OF. Small peaks appear due to the ion-ion contribution to the force. However, with fixed bulk ions and a constant projectile velocity, these peaks and valleys do not affect the average stopping power.

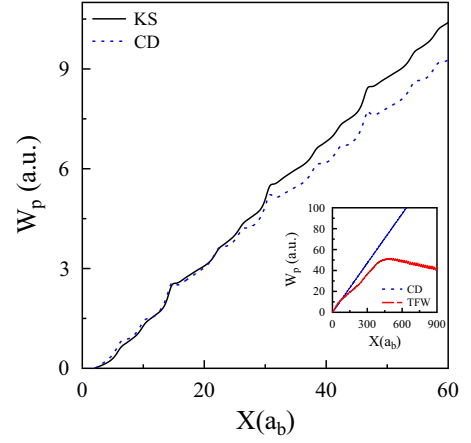


FIG. 7. Work on the deuteron projectile as a function of distance traveled.  $v_p = 2.5 a.u.$  and  $\delta t = 0.29 a.s.$  Linear fit to this line gives the electronic stopping power (ESP). time-dependent (TD) Kohn-Sham (black solid), Current-dependent TD orbital-free (CD) (blue dotted). Inset: Long trajectory shows instability (a deviation of linearity) for the TFW TD orbital-free (red dashed). For TFW  $\delta t = 0.096 a.s.$

The inset of Fig. 7 also shows the TFW TD-OF-DFT. Numerical instability leading to a nonlinear work for the TFW. For high projectile velocities,  $v_p \gg v_F = (3\pi^2\rho)^{\frac{1}{3}}$  the stopping power can be fit before dynamics become unstable. In this regime the required time step is determined by the projectile velocity, not the electron dynamics. This is the case for the trajectory shown in Fig. 7. For low velocities,  $v_p \leq v_F$ , the electron dynamics determines the required time step. In this regime, the TFW method requires very small time steps,  $\sim 10$  times lower (max  $\delta t = 0.096 a.s.$ ) than KS or CD (max  $\delta t = 0.96 a.s.$ ), in order to maintain linearity and extract a reasonable fit for the stopping power. By comparison the current-dependent orbital-free shows no signs of instability.

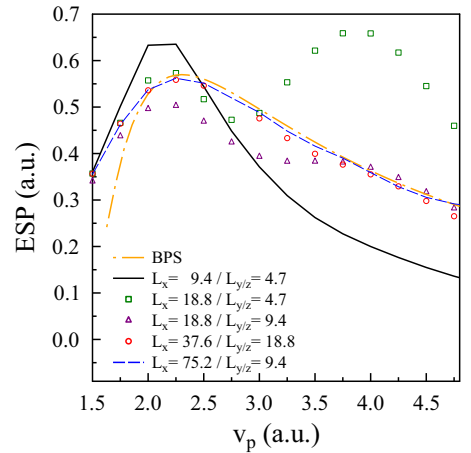


FIG. 8. 3.5 g/cc, 100 kK deuterium stopping power for deuteron. Convergence of TD-OF-DFT result with respect to the dimensions of the periodic simulation cell. BPS result also shown for reference. Length shown in Bohr. See text for description.

### APPENDIX C: CONVERGENCE OF TD-OF-DFT WITH RESPECT TO SIMULATION CELL SIZE

As we have mentioned in the main text, large simulation box sizes are required to converge high-velocity stopping power. This can be prohibitive for TD-KS-DFT simulations, especially at high temperatures. However, for the increased efficiency for TD-OF-DFT does allow one to reach the required large box sizes. In Fig. 8 we show the stopping power for various box sizes and shapes. All simulations are for a deuteron projectile stopped by 3.5 g/cc bulk deuterium at 10 kilo-Kelvin. This is similar to the simulations shown in Fig. 5. To separate convergence with box size, vs. convergence with respect to ion configurations, we use periodic replicas of a base cell, i.e., increased cell size only changes the electron response not the initial electron density. Note that in Fig. 3 we use a cubic cell of 128 atoms. This is well converged with respect to the directions perpendicular to the projectile velocity, but not with the parallel direction.

Results from the smallest box, the base cell, are shown as a black line. The base cell only includes 32 atoms in a  $2 \times 1 \times 1$  xyz aspect ratio; the projectile velocity is parallel to the  $x$  direction. The base cell is replicated in the  $x$  direction,

leading to a  $4 \times 1 \times 1$  aspect ratio, leads to the green squares. The large overestimation of stopping power near  $v_p \sim 4.0$  may be a resonance between the  $x$  length, the  $y/z$  lengths and  $v_p$  resulting in strong interaction of the projectile with its own wake. Replicating the base cell once in all directions leads to the purple triangles ( $4 \times 2 \times 2$ ). Replicating the base cell four times in each direction ( $8 \times 4 \times 4$ ) leads to the red circles, which no longer show oscillations. Finally, replicating the base cell eight times in the  $x$  direction and twice in the  $y/z$  directions ( $16 \times 2 \times 2$ ) gives the converged blue dashed line. This shows that  $y/z$  convergence is achieved with relatively short lengths, but the box requires long lengths parallel to the projectile velocity. The analytical BPS result, based on homogeneous electron density (orange dash-dot line) is also shown for reference.

Considering the excellent agreement between the OF and KS TD-DFT results at high velocity, shown throughout this paper, we expect that a similar convergence analysis would apply to the TD-KS-DFT results. This could have implications on multiple studies of TD-KS-DFT stopping power for low-temperature condensed phase systems, where a suppressed high-velocity tail has been observed, but additional factors should be considered [23,47].

- 
- [1] H. F. W. Sadrozinski, V. Bashkurov, B. Keeney, L. R. Johnson, S. G. Peggs, G. Ross, T. Satogata, R. W. M. Schulte, A. Seiden, K. Shanazi *et al.*, *IEEE Trans. Nucl. Sci.* **51**, 3 (2004).
- [2] W. D. Newhauser and R. Zhang, *Phys. Med. Bio.* **60**, R155 (2015).
- [3] W. Donahue, W. D. Newhauser, and J. F. Ziegler, *Phys. Med. Bio.* **61**, 6570 (2016).
- [4] H. Tai, H. Bichsel, J. W. Wilson, J. L. Shinn, F. A. Cucinotta, and F. F. Badavi, NASA Tech. Rep. No. 19970036323, 1997.
- [5] G. Fuchs, F. Studer, E. Balanzat, D. Groult, M. Toulemonde, and J. C. Jousset, *Europhys. Lett.* **3**, 321 (1987).
- [6] C.-K. Li and R. D. Petrasso, *Phys. Rev. Lett.* **70**, 3059 (1993).
- [7] G. Maynard and C. Deutsch, *Phys. Rev. A* **26**, 665 (1982).
- [8] S. Skupsky, *Phys. Rev. A* **16**, 727 (1977).
- [9] A. B. Zylstra, J. A. Frenje, P. E. Grabowski, C. K. Li, G. W. Collins, P. Fitzsimmons, S. Glenzer, F. Graziani, S. B. Hansen, S. X. Hu *et al.*, *Phys. Rev. Lett.* **114**, 215002 (2015).
- [10] D. Wu, X. T. He, W. Yu, and S. Fritzsche, *Phys. Rev. E* **95**, 023207 (2017).
- [11] J. A. Frenje, P. E. Grabowski, C. K. Li, F. H. Séguin, A. B. Zylstra, M. Gatu Johnson, R. D. Petrasso, V. Y. Glebov, and T. C. Sangster, *Phys. Rev. Lett.* **115**, 205001 (2015).
- [12] J. Frank, A. King, and D. Raine, *Accretion Power in Astrophysics* (Cambridge University Press, Cambridge, 2002).
- [13] K. Nordlund, *Comput. Mater. Sci.* **3**, 448 (1995).
- [14] L. S. Brown, D. L. Preston, and R. L. S. Jr., *Phys. Rep.* **410**, 237 (2005).
- [15] N. R. Arista and A. R. Piriz, *Phys. Rev. A* **35**, 3450 (1987).
- [16] C. F. Clouser and N. R. Arista, *Phys. Rev. E* **97**, 023202 (2018).
- [17] Z. G. Fu, Z. Wang, and P. Zhang, *Phys. Plasmas* **24**, 112710 (2017).
- [18] R. J. Mathar, J. R. Sabin, and S. Trickey, *Nucl. Instrum. Methods Phys. Res. B* **155**, 249 (1999).
- [19] R. J. Mathar, S. Trickey, and J. R. Sabin, in *Theory of the Interaction of Swift Ions with Matter. Part I*, Vol. 45 of Advances in Quantum Chemistry (Academic Press, New York, 2004), pp. 277–288.
- [20] M. Quijada, A. G. Borisov, I. Nagy, R. Díez Muiño, and P. M. Echenique, *Phys. Rev. A* **75**, 042902 (2007).
- [21] R. J. Magyar, L. Shulenburg, and A. D. Baczewski, *Contrib. Plasma Phys.* **56**, 459 (2016).
- [22] G. Bi, J. Kang, and L.-W. Wang, *Phys. Chem. Chem. Phys.* **19**, 9053 (2017).
- [23] D. C. Yost, Y. Yao, and Y. Kanai, *Phys. Rev. B* **96**, 115134 (2017).
- [24] C.-k. Li, F. Mao, F. Wang, Y.-l. Fu, X.-p. Ouyang, and F.-S. Zhang, *Phys. Rev. A* **95**, 052706 (2017).
- [25] C.-K. Li, F. Wang, B. Liao, X.-P. OuYang, and F.-S. Zhang, *Phys. Rev. B* **96**, 094301 (2017).
- [26] K. G. Reeves, Y. Yao, and Y. Kanai, *Phys. Rev. B* **94**, 041108 (2016).
- [27] D. C. Yost and Y. Kanai, *Phys. Rev. B* **94**, 115107 (2016).
- [28] E. E. Quashie, B. C. Saha, and A. A. Correa, *Phys. Rev. B* **94**, 155403 (2016).
- [29] W. Kohn and L. J. Sham, *Phys. Rev.* **140**, A1133 (1965).
- [30] N. D. Mermin, *Phys. Rev.* **137**, A1441 (1965).
- [31] A. D. Baczewski, L. Shulenburg, M. P. Desjarlais, S. B. Hansen, and R. J. Magyar, *Phys. Rev. Lett.* **116**, 115004 (2016).
- [32] A. Pribram-Jones, P. E. Grabowski, and K. Burke, *Phys. Rev. Lett.* **116**, 233001 (2016).
- [33] L. Burakovsky, C. Ticknor, J. D. Kress, L. A. Collins, and F. Lambert, *Phys. Rev. E* **87**, 023104 (2013).
- [34] J. Kress, J. S. Cohen, D. Kilcrease, D. Horner, and L. Collins, *High Energy Density Phys.* **7**, 155 (2011).
- [35] V. V. Karasiev, T. Sjoström, and S. Trickey, *Comput. Phys. Commun.* **185**, 3240 (2014).

- [36] V. V. Karasiev and S. B. Trickey, in *Concepts of Mathematical Physics in Chemistry: A Tribute to Frank E. Harris - Part A*, Vol. 71 of *Advances in Quantum Chemistry*, edited by J. R. Sabin and R. Cabrera-Trujillo (Academic Press, New York, 2015), pp. 221–245.
- [37] J. Lehtomäki, I. Makkonen, M. A. Caro, A. Harju, and O. Lopez-Acevedo, *J. Chem. Phys.* **141**, 234102 (2014).
- [38] M. Chen, X.-W. Jiang, H. Zhuang, L.-W. Wang, and E. A. Carter, *J. Chem. Theory Comput.* **12**, 2950 (2016).
- [39] A. J. White, L. A. Collins, J. D. Kress, C. Ticknor, J. Clérrouin, P. Arnault, and N. Desbiens, *Phys. Rev. E* **95**, 063202 (2017).
- [40] C. Ticknor, J. D. Kress, L. A. Collins, J. Clérrouin, P. Arnault, and A. Decoster, *Phys. Rev. E* **93**, 063208 (2016).
- [41] C. Ticknor, L. A. Collins, and J. D. Kress, *Phys. Rev. E* **92**, 023101 (2015).
- [42] C. Ticknor, S. D. Herring, F. Lambert, L. A. Collins, and J. D. Kress, *Phys. Rev. E* **89**, 013108 (2014).
- [43] J. D. Kress, J. S. Cohen, D. P. Kilcrease, D. A. Horner, and L. A. Collins, *Phys. Rev. E* **83**, 026404 (2011).
- [44] J. D. Kress, J. S. Cohen, D. A. Horner, F. Lambert, and L. A. Collins, *Phys. Rev. E* **82**, 036404 (2010).
- [45] D. A. Horner, F. Lambert, J. D. Kress, and L. A. Collins, *Phys. Rev. B* **80**, 024305 (2009).
- [46] S. X. Hu, L. A. Collins, V. N. Goncharov, J. D. Kress, R. L. McCrory, and S. Skupsky, *Phys. Rev. E* **92**, 043104 (2015).
- [47] A. Schleife, Y. Kanai, and A. A. Correa, *Phys. Rev. B* **91**, 014306 (2015).
- [48] Y. A. Wang and E. A. Carter, *Orbital-Free Kinetic-Energy Density Functional Theory* (Springer Netherlands, Dordrecht, 2002), pp. 117–184.
- [49] Y. A. Wang, N. Govind, and E. A. Carter, *Phys. Rev. B* **60**, 16350 (1999).
- [50] Y. Ke, F. Libisch, J. Xia, and E. A. Carter, *Phys. Rev. B* **89**, 155112 (2014).
- [51] F. Perrot, *Phys. Rev. A* **20**, 586 (1979).
- [52] P. K. Acharya, L. J. Bartolotti, S. B. Sears, and R. G. Parr, *Proc. Nat. Acad. Sci. U.S.A.* **77**, 6978 (1980).
- [53] L. W. Wang and M. P. Teter, *Phys. Rev. B* **45**, 13196 (1992).
- [54] T. Sjöström and J. Daligault, *Phys. Rev. B* **88**, 195103 (2013).
- [55] D. Neuhauser, S. Pistinner, A. Coomar, X. Zhang, and G. Lu, *J. Chem. Phys.* **134**, 144101 (2011).
- [56] H. Xiang, M. Zhang, X. Zhang, and G. Lu, *J. Phys. Chem. C* **120**, 14330 (2016).
- [57] J. P. Perdew and A. Zunger, *Phys. Rev. B* **23**, 5048 (1981).
- [58] W. Jones and W. H. Young, *J. Phys. C* **4**, 1322 (1971).
- [59] H. Jiang and W. Yang, *J. Chem. Phys.* **121**, 2030 (2004).
- [60] E. Madelung, *Naturwissenschaften* **14**, 1004 (1926).
- [61] E. Runge and E. K. U. Gross, *Phys. Rev. Lett.* **52**, 997 (1984).
- [62] A. Domsps, P.-G. Reinhard, and E. Suraud, *Phys. Rev. Lett.* **80**, 5520 (1998).
- [63] Z. A. Moldabekov, M. Bonitz, and T. S. Ramazanov, *Phys. Plasmas* **25**, 031903 (2018).
- [64] G. Giuliani and G. Vignale, *Quantum Theory of the Electron Liquid* (Cambridge University Press, Cambridge, 2008).
- [65] I. Tokatly and O. Pankratov, *Phys. Rev. B* **60**, 15550 (1999).
- [66] N. Crouseilles, P.-A. Hervieux, and G. Manfredi, *Phys. Rev. B* **78**, 155412 (2008).
- [67] C. Ciraci and F. Della Sala, *Phys. Rev. B* **93**, 205405 (2016).
- [68] C. Ciraci, *Phys. Rev. B* **95**, 245434 (2017).
- [69] V. B. Gildenburg and I. A. Pavlichenko, *Phys. Plasmas* **24**, 084502 (2017).
- [70] V. U. Nazarov, J. M. Pitarke, C. S. Kim, and Y. Takada, *Phys. Rev. B* **71**, 121106 (2005).
- [71] V. U. Nazarov, J. M. Pitarke, Y. Takada, G. Vignale, and Y. C. Chang, *Phys. Rev. B* **76**, 205103 (2007).
- [72] A. A. Correa, *Comput. Mater. Sci.* **150**, 291 (2018).
- [73] X. Gonze, B. Amadon, P.-M. Anglade, J.-M. Beuken, F. Bottin, P. Boulanger, F. Bruneval, D. Caliste, R. Caracas, M. Côté *et al.*, *Comput. Phys. Commun.* **180**, 2582 (2009).
- [74] Y. Ding, A. J. White, S. X. Hu, O. Certik, and L. A. Collins, *Phys. Rev. Lett.* (to be published 2018).
- [75] F. Lambert, J. Clérrouin, and G. Zerah, *Phys. Rev. E* **73**, 016403 (2006).
- [76] A. Ojanperä, A. V. Krasheninnikov, and M. Puska, *Phys. Rev. B* **89**, 035120 (2014).
- [77] R. Ullah, E. Artacho, and A. A. Correa, *Phys. Rev. Lett.* **121**, 116401 (2018).